COMPUTATIONAL EVALUATION OF THERMAL BARRIER COATINGS

Kevin Irick
The University of New Mexico
Albuquerque, NM, USA

Nima Fathi
The University of New Mexico
Albuquerque, NM, USA

ABSTRACT

In the power plant industry, the turbine inlet temperature (TIT) plays a key role in the efficiency of the gas turbine and, therefore, the overall—in most cases combined—thermal power cycle efficiency. Gas turbine efficiency increases by increasing TIT. However, an increase of TIT would increase the turbine component temperature which can be critical (e.g., hot gas attack). Thermal barrier coatings (TBCs)—porous media coatings—can avoid this case and protect the surface of the turbine blade. This combination of TBC and film cooling produces a better cooling performance than conventional cooling processes. The effective thermal conductivity of this composite is highly important in design and other thermal/structural assessments. In this article, the effective thermal conductivity of a simplified model of TBC is evaluated. This work details a numerical study on the steady-state thermal response of two-phase porous media in two dimensions using personal finite element analysis (FEA) code. Specifically, the system response quantity (SRQ) under investigation is the dimensionless effective thermal conductivity of the domain. A thermally conductive matrix domain is modeled with a thermally conductive circular pore arranged in a uniform packing configuration. Both the pore size and the pore thermal conductivity are varied over a range of values to investigate the relative effects on the SRQ. In this investigation, an emphasis is placed on using code and solution verification techniques to evaluate the obtained results. The method of manufactured solutions (MMS) was used to perform code verification for the study, showing the FEA code to be second-order accurate. Solution verification was performed using the grid convergence index (GCI) approach with the global deviation uncertainty estimator on a series of five systematically refined meshes for each porosity and thermal conductivity model configuration. A comparison of the SRQs across all domain configurations is made, including uncertainty derived through the GCI analysis.

NOMENCLATURE

A	= area
α	= porosity
ε	= error
FS	= factor of safety
$\boldsymbol{G}$	= conductance matrix
Γ	= domain boundary
h	= characteristic mesh size
H	= mesh number
i	= index
k	= thermal conductivity
$\boldsymbol{K}$	= thermal conductivity matrix
L	= cell length
N	= total quantity
$\boldsymbol{N}$	= shape function
Ω	= domain
p	= order of accuracy
$\boldsymbol{P}$	= vertex heat load vector
$\boldsymbol{q}$	= heat flux vector
Q	= heat flow per unit length
r	= mesh ratio
R	= void radius
ρ	= energy balance residual
$\boldsymbol{\rho}$	= energy balance residual vector
S	= energy source
T	= temperature
$\boldsymbol{T}$	= triangle vertex temperature vector
u	= system response quantity
U	= uncertainty
W	= cell half-width
x	= x-coordinate
y	= y-coordinate

Subscripts

C	= cold

1

eff	= effective
f	= formal
H	= mesh number, hot
i	= index
j	= index
L∞	= L_∞ norm
MMS	= manufactured solution
n	= normal
num	= numerical
O	= observed
t	= triangle, transcendental
v	= vertex
x	= x-direction
y	= y-direction

Superscripts

*	= dimensionless, global

1. INTRODUCTION

The future of increased efficiency in gas turbine-driven power plant energy generation is heavily dependent on the increased temperature of the turbine inlet temperature (TIT) [1-4]. In spite of the pursuit of higher TIT levels, virgin metal material in the turbine components are susceptible to a variety of aggressive and high-consequence degradation or failure modes. Such issues include accelerated thermal creep, material degradation due to oxidation, and cycle fatigue [5,6]. Thermal-related corrosion issues arise at various temperature levels anywhere in the range of 650-1700 °C [2,7-11].

To mitigate thermal issues, thermal barrier coatings (TBCs) are used to protect the virgin material. Such coatings, including spray technologies are typically comprised of some form of ceramic composite material [12-14]. These composite materials are porous in nature and provide significant protection to the metal turbine components to allow for better overall performance and efficiency.

Understanding the thermophysical properties of TBC materials is critical to the design and advancement of gas turbines for plant power generation for current and future installations. As systems continue to produce higher TIT levels, the thermal performance of advanced TBCs becomes more critical. This investigation evaluates the effective thermal transport in simplified models of TBC porous structures, specifically two-phase porous media, as an initial study into TBC material nano-structure effective thermal response.

2. SYSTEM DESCRIPTION

In order to analyze the thermal transport phenomena within the TBC as a part the authors' efforts, a two-dimensional system is constructed, consistent with the illustration given in Figure 1. For this study, a unit half-cell is given with height, *L*, and width, *W*, and is oriented in the Cartesian ***x-y*** plane with unit thickness out-of-plane. The bulk matrix material is defined as the first material phase with thermal conductivity k_1, where

the pore phase is defined to have thermal conductivity k_2. The pore pattern is circular, centered in the unit cell, with radius, *R*. Both the *x*=0 and *x*=*W* boundaries are given periodic boundary conditions for system symmetry, and the *y*=0 and *y*=*L* boundaries have enforced hot and cold boundary temperatures, T_H and T_C, respectively. By enforcing Dirichlet boundary conditions at the hot and cold boundaries, heat flow—per unit length—is induced in the positive *y*-direction, perpendicular to each boundary, indicated by Q_H and Q_C, respectively.
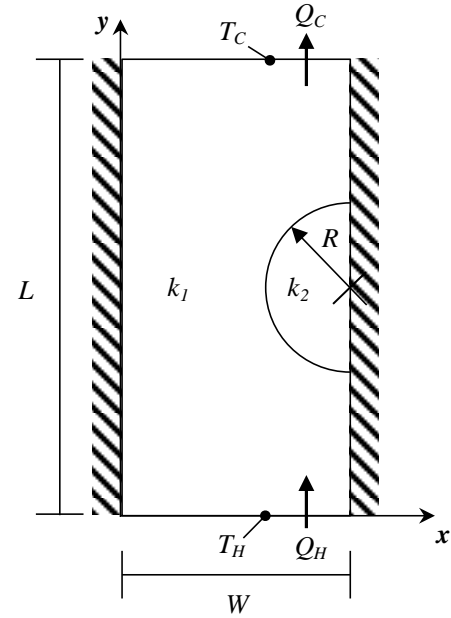

Figure 1. Unit half-cell nano-porous structure

Of interest in this work is the effect of relative pore size and relative pore thermal conductivity on the overall effective thermal conductivity, k_{eff}, of the TBC. Thus, the dimensionless parameter, porosity, *α*, is used to define the relative pore size, where

$$\alpha = (\pi R^2)/(2WL) \qquad (1)$$

The k_{eff} value is defined by overall heat flow through the system and the enforced boundary temperatures such that

$$k_{eff} = [(Q_H + Q_C)L]/[2W(T_H - T_C)]. \qquad (2)$$

where the domain is assumed to have unit thickness out-of-plane.

In theory, $Q_H=Q_C$, but because this study is numerical in nature, the average of the two heat flow values is used in Eq. (2) to define the overall induced heat flow through the domain. To account for variable material properties of the matrix and porous phases in different TBCs, the ultimate system response quantity (SRQ) of interest in this analysis is the dimensionless effective thermal conductivity, *k**, which is merely the ratio of

the effective thermal conductivity with the matrix material thermal conductivity, simply evaluated as

$$k^* = k_{eff}/k_1. \tag{3}$$

This study will show the effects on the SRQ of varying the k_2-to-k_1 ratio along with varying the α, using numerical verification techniques to quantify uncertainty in that value. Ratios in the two-phase thermal conductivities are evaluated from 0 to 2, and α values are varied from 5% to 65%.

3. NUMERICAL APPROACH

3.1 DISCRETIZATION

In order to determine the SRQ, the temperature distribution, T, and resultant heat source terms, S, must be solved to satisfy the governing partial differential equation (PDE), the heat equation, as expressed in Eq. (4), where k is the thermal conductivity.

$$k\left(\frac{\partial^2 T}{\partial x^2} + \frac{\partial^2 T}{\partial y^2}\right) + S = 0 \tag{4}$$

To numerically discretize the heat equation, unstructured triangular meshes were generated over the domain within each material phase. To accommodate the verification approaches used in this study, systematically refined meshes were generated for each porosity level, an example of which is shown in Figure 2a through Figure 2e, for mesh number, H, 5 through 1, respectively. Likewise, the finest meshes for a selection of porosity models of 5%, 25%, 45%, and 65% are given in Figure 3a through Figure 3d, respectively.
Each tth triangle is configured with three vertices such that the ith vertex is located at $(x_{t,i}, y_{t,i})$ with temperature $T_{t,I}$ and area A_t, is shown in

 Figure 4. Each Hth mesh for a given porosity level is then described with a characteristic mesh size h_H. If $N_{H,t}$ is the total number of triangles in mesh H, then

$$h_H = \sqrt{\frac{1}{N_H}\Sigma_{t=1}^{N_{H,}}A_t} \tag{5}$$

Thus, systematic mesh refinement here approximately halves the characteristic mesh size from mesh $H+1$ to mesh H.

The domain discretization is used with a second order accurate Galerkin Finite Element Method (FEM) approach which is employed to solve Eq. (4) over the entire domain [15]. In short, Eq. (4) can be solved over each element, individually, using the discretized PDE matrix equation

$$\int_\Omega (\nabla N)^T K \nabla N d\Omega T = \int_\Omega N^T S d\Omega - \int_\Gamma N^T q_n d\Gamma \tag{6}$$

where N is the linear shape function row vector used to interpolate field variables across a single element, K is the 2x2

thermal conductivity matrix, T is the vector of triangle vertex temperature values, q_n, is the boundary normal heat flux on a triangle boundary, Ω is the element domain, and Γ is the element boundary.

Furthermore, the different parts of Eq. (6) are condensed and defined as the conductance matrix, G, and the heat load matrix P, where
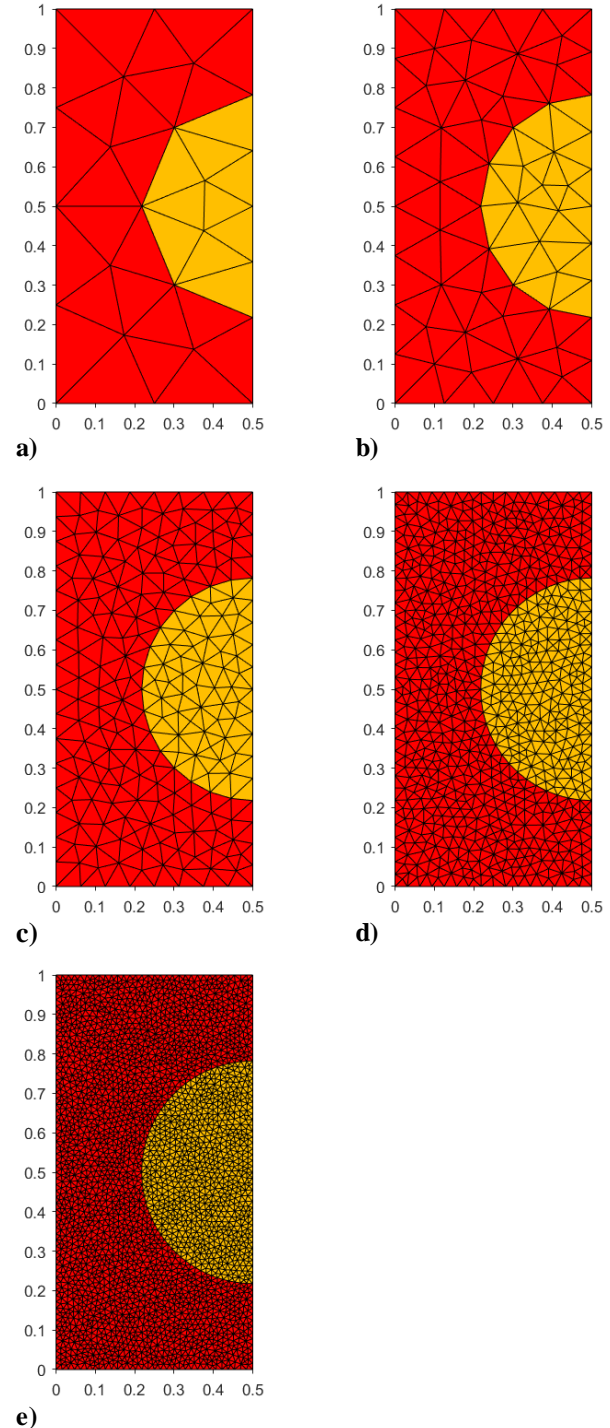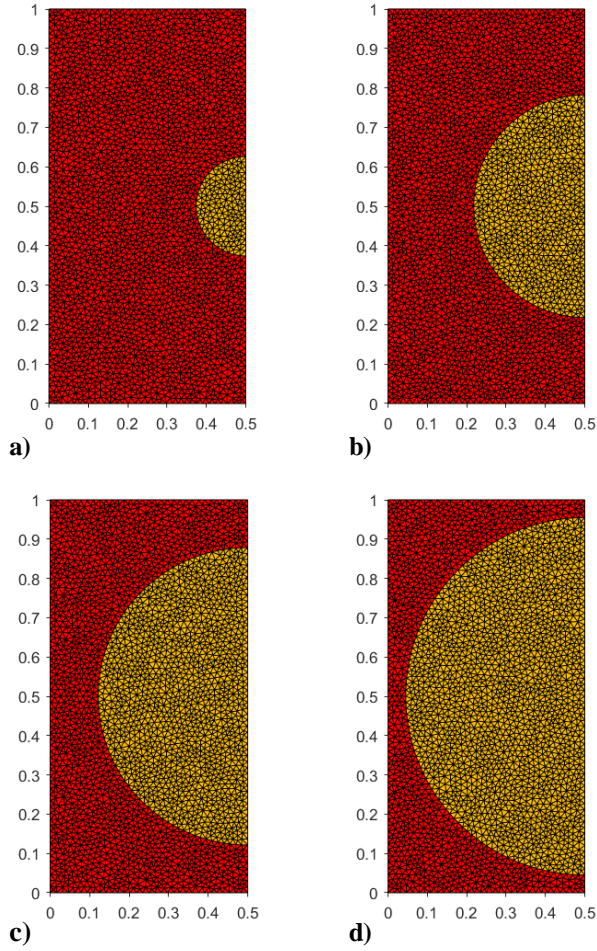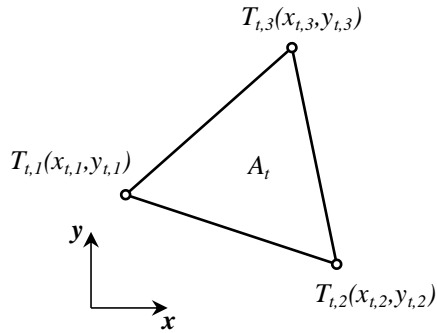

a)

b)

c)

d)

e)

Figure 2. Systematic mesh refinement for α=25%

a)   b)

c)   d)

Figure 3. Finest mesh for varying porosity levels

Figure 4. Notional linear triangle element

$$G = \int_{\Omega} (\nabla N)^T K \nabla N d\Omega \qquad (7)$$

and

$$P = \int_{\Omega} N^T S d\Omega - \int_{\Gamma} N^T q_n d\Gamma \qquad (8)$$

such that

$$GT = P. \qquad (9)$$

3.2 SOLVER

The meshes employed in this study were generated using open-source Gmsh software [16]. The custom code used for this study was written in Fortran as a generic two-dimensional FEM heat transfer solver. A basic successive over-relaxation method was used to iteratively update solutions to Eq. (9) until some residual level exit criteria was met.

The residual vector, ρ, for the system is computed as

$$\rho = GT - P \qquad (10)$$

where the L_∞ norm residual, $\rho_{L\infty}$, defined as

$$\rho_{L\infty} = \max|\rho|. \qquad (11)$$

A $\rho_{L\infty}$ value of 10^{-8} was used as exit criteria for solution completion.

4. VERIFICATION APPROACH

4.1 CODE VERIFICATION

In order to verify the formally second order accurate solution, the Method of Manufactured Solutions (MMS) was employed [17,18]. The MMS approach allows for a user-defined temperature distribution to be selected, T_{MMS}, where the operator—in this case defined by the PDE in Eq. (4)—acts on the manufactured solution. The resulting source term, S_{MMS}, falls out of the operator, where

$$S_{MMS} = -k \left(\frac{\partial^2 T}{\partial x^2} + \frac{\partial^2 T_{MMS}}{\partial y^2} \right). \qquad (12)$$

Thus, by applying S_{MMS} and the boundary conditions that satisfy T_{MMS} to the domain, the solved system of equations should converge to T_{MMS} with mesh refinement. Here, T_{MMS} is defined as

$$T_{MMS}(x,y) = \cos(2\pi x)\sin(\pi y + 0.75) \qquad (13)$$

and is applied as a boundary condition at *y=0* and *y=L* as Dirichlet conditions. It follows that the first partial derivatives are given to be

4

$$\frac{\partial T_{MMS}}{\partial x} = -2\pi \sin(2\pi x) \sin(\pi y + 0.75) \tag{14}$$

$$\frac{\partial T_{MMS}}{\partial y} = \pi \cos(2\pi x) \cos(\pi y + 0.75)$$

and are enforced at the boundaries where *x=0* and *x=W* as Neumann boundary conditions. The resulting source term distribution is then

$$S_{MMS} = 5\pi^2 k \cos(2\pi x) \sin(\pi y + 0.75). \tag{15}$$

For this study, the L_∞ norm metric is used on temperature error, $\varepsilon_{MMS,H}$, over all N_v vertices in mesh H, where

$$\epsilon_{MMS,H} = \max_i |T_i - T_{MMS,i}| \tag{16}$$

based on the solution temperature, T_i, of the ith vertex. The observed order of accuracy for mesh H, $p_{O,H}$, is determined by

$$p_{O,H} = \ln(\epsilon_{MMS,H}/\epsilon_{MMS,H+1}) / \ln(h_H/h_{H+1}). \tag{17}$$

4.2 SOLUTION VERIFICATION

The numerical error, U_{num}, for the SRQ, k^*, is approximated in this method by performing solution verification using a modern version of a more traditional grid convergence index (GCI) [18,19] approach that incorporates a global deviation estimator for the solution [20]. This approach uses an empirical trend to scale a factor of safety, FS, for U_{num} based on how closely the convergent observed order of accuracy is to the formal order of accuracy, thus acknowledging how close the solution is to the asymptotic solution region.

The modified transcendental order of accuracy, p_t, used for this study is given by

$$p_t = \ln\left[(r_{1,2}^{p_t} - 1)\left(\left|\frac{u_3-u}{u_2-u_1}\right|\right) + r_{1,2}^{p_t}\right] / \ln(r_{1,2}r_{2,3}) \tag{18}$$

where u_H represents the SRQ of interest as computed on mesh H, and

$$r_{i,j} = h_j/h_i. \tag{19}$$

For this problem, where the SRQ is k^*, the global deviation parameter, $\varDelta p$, is computed as

$$\varDelta p = \min(|p_f - p_t|, 4p_f, 0.95p_f) \tag{20}$$

with p_f being the formal order of accuracy of the solution method which, in this study, is 2. Lastly, the global order of accuracy, p^*, used to compute the global deviation GCI FS is

$$p^* = p_f - \varDelta p \tag{21}$$

such that

$$FS = 3 - 1.9(p^*/p_f)^8 \tag{22}$$

This FS value is then used to estimate the numerical uncertainty on the fine mesh SRQ solution, where

$$U_{num} = FS \left|(u_2 - u_1)/\left(r_{1,2}^{p^*} - 1\right)\right| \tag{23}$$

5. RESULTS AND DISCUSSION

5.1 CODE VERIFICATION

Using the MMS solution and conditions described in Eq. (13) through Eq. (15) to perform the MMS verification, the trends of logarithmic error against logarithmic mesh size are shown in Figure 5, where the trend of a formal second order accurate solution is also shown in qualitative comparison. Likewise, Figure 6 shows the convergence of the observed order of accuracy with respect to mesh number.
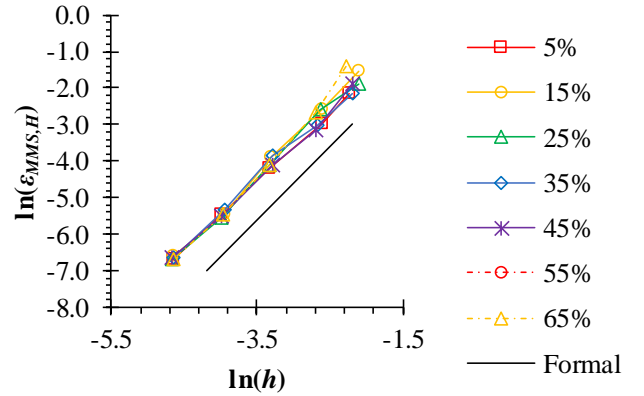

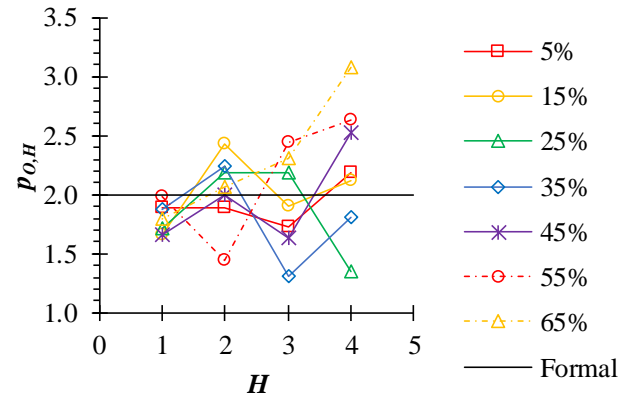
Figure 5. MMS error trend with mesh refinement

Figure 6. MMS observed order of accuracy convergence

Table 1 through Table 7 detail the specific mesh refinement and MMS observed order of accuracy parameters, showing an approximately second order accurate scheme.

5

Table 1. Systematic mesh refinement and MMS observed order of accuracy parameters for α=5%

H	$r_{H,H+1}$	$\ln(h_H)$	$\ln(\varepsilon_{MMS,H})$	$p_{O,H}$
5	---	-2.24	-2.15	---
4	1.46	-2.62	-2.98	2.18
3	2.05	-3.34	-4.22	1.73
2	1.93	-3.99	-5.46	1.89
1	1.93	-4.65	-6.71	1.89

Table 2. Systematic mesh refinement and MMS observed order of accuracy parameters for α=15%

H	$r_{H,H+1}$	$\ln(h_H)$	$\ln(\varepsilon_{MMS,H})$	$p_{O,H}$
5	---	-2.11	-1.53	---
4	1.66	-2.62	-2.60	2.11
3	1.99	-3.31	-3.91	1.90
2	1.90	-3.95	-5.46	2.42
1	2.02	-4.65	-6.62	1.65

Table 3. Systematic mesh refinement and MMS observed order of accuracy parameters for α=25%

H	$r_{H,H+1}$	$\ln(h_H)$	$\ln(\varepsilon_{MMS,H})$	$p_{O,H}$
5	---	-2.11	-1.87	---
4	1.70	-2.64	-2.59	1.35
3	2.01	-3.34	-4.12	2.19
2	1.92	-3.99	-5.54	2.18
1	1.96	-4.67	-6.69	1.71

Table 4. Systematic mesh refinement and MMS observed order of accuracy parameters for α=35%

H	$r_{H,H+1}$	$\ln(h_H)$	$\ln(\varepsilon_{MMS,H})$	$p_{O,H}$
5	---	-2.19	-2.15	---
4	1.61	-2.67	-3.02	1.80
3	1.88	-3.30	-3.84	1.31
2	1.93	-3.96	-5.32	2.25
1	2.01	-4.65	-6.63	1.88

Table 5. Systematic mesh refinement and MMS observed order of accuracy parameters for α=45%

H	$r_{H,H+1}$	$\ln(h_H)$	$\ln(\varepsilon_{MMS,H})$	$p_{O,H}$
5	---	-2.19	-1.89	---
4	1.64	-2.69	-3.15	2.52
3	1.81	-3.28	-4.11	1.63
2	2.03	-3.99	-5.52	1.99
1	1.97	-4.67	-6.65	1.66

Table 6. Systematic mesh refinement and MMS observed order of accuracy parameters for α=55%

H	$r_{H,H+1}$	$\ln(h_H)$	$\ln(\varepsilon_{MMS,H})$	$p_{O,H}$
5	---	-2.19	-1.54	---
4	1.67	-2.71	-2.89	2.63
3	1.80	-3.29	-4.32	2.44
2	2.01	-3.99	-5.33	1.44
1	1.95	-4.66	-6.65	1.98

Table 7. Systematic mesh refinement and MMS observed order of accuracy parameters for α=65%

H	$r_{H,H+1}$	$\ln(h_H)$	$\ln(\varepsilon_{MMS,H})$	$p_{O,H}$
5	---	-2.28	-1.39	---
4	1.53	-2.71	-2.70	3.08
3	1.86	-3.32	-4.13	2.31
2	1.91	-3.97	-5.45	2.06
1	1.98	-4.65	-6.68	1.79

5.2 SOLUTION VERIFICATION

As mentioned previously, k^* is computed using the average numerically-produced values of Q_H and Q_C, as described by Eq. (2) and Eq. (3). These heat flow values are computed by summing the residual values, implied from Eq. (10), of all vertices on the Q_H and Q_C boundaries where T_H and T_C are enforced, respectively.

After performing the solution verification procedures described with Eq. (18) through Eq. (23), the following tables show the computed global deviation parameters and ultimate U_{num} approximation for the finest mesh in each material configuration model. Note that the U_{num} values given in these tables are expressed as percent values relative to the presented fine mesh k^* values. All U_{num} values are obtained to be less than 0.2% of the fine mesh k^* values.

Table 8. Global deviation GCI parameters for α=5%

k_2/k_1	k^*	$r_{1,2}$	p_t	Δp	p^*	FS	U_{num}
0.00	0.91	1.93	1.68	0.32	1.68	2.52	0.147%
0.25	0.94	1.93	1.67	0.33	1.67	2.54	0.072%
0.50	0.97	1.93	1.66	0.34	1.66	2.57	0.034%
0.75	0.99	1.93	1.64	0.36	1.64	2.61	0.013%
1.00	1.00	1.93	0.00	1.90	0.10	3.00	0.000%
1.25	1.01	1.93	1.60	0.40	1.60	2.68	0.008%
1.50	1.02	1.93	1.57	0.43	1.57	2.72	0.014%
1.75	1.03	1.93	1.55	0.45	1.55	2.75	0.018%
2.00	1.03	1.93	1.52	0.48	1.52	2.79	0.021%

Table 9. Global deviation GCI parameters for α=15%

k_2/k_1	k^*	$r_{1,2}$	p_t	Δp	p^*	FS	U_{num}
0.00	0.74	2.02	1.89	0.11	1.89	1.79	0.097%
0.25	0.84	2.02	1.88	0.12	1.88	1.82	0.047%
0.50	0.90	2.02	1.88	0.12	1.88	1.85	0.023%
0.75	0.96	2.02	1.87	0.13	1.87	1.89	0.009%
1.00	1.00	2.02	0.00	1.90	0.10	3.00	0.000%
1.25	1.03	2.02	1.86	0.14	1.86	1.96	0.006%
1.50	1.06	2.02	1.85	0.15	1.85	1.99	0.009%
1.75	1.09	2.02	1.84	0.16	1.84	2.02	0.012%
2.00	1.11	2.02	1.83	0.17	1.83	2.06	0.014%

Table 10. Global deviation GCI parameters for α=25%

k_2/k_1	k^*	$r_{1,2}$	p_t	Δp	p^*	FS	U_{num}
0.00	0.60	1.96	1.91	0.09	1.91	1.70	0.095%
0.25	0.74	1.96	1.91	0.09	1.91	1.70	0.044%
0.50	0.85	1.96	1.91	0.09	1.91	1.71	0.020%
0.75	0.93	1.96	1.90	0.10	1.90	1.72	0.007%
1.00	1.00	1.96	0.06	1.90	0.10	3.00	0.000%
1.25	1.06	1.96	1.90	0.10	1.90	1.74	0.004%
1.50	1.11	1.96	1.90	0.10	1.90	1.75	0.007%
1.75	1.15	1.96	1.89	0.11	1.89	1.77	0.009%
2.00	1.18	1.96	1.89	0.11	1.89	1.78	0.010%

Table 11. Global deviation GCI parameters for α=35%

k_2/k_1	k^*	$r_{1,2}$	p_t	Δp	p^*	FS	U_{num}
0.00	0.48	2.01	1.95	0.05	1.95	1.45	0.090%
0.25	0.65	2.01	1.94	0.06	1.94	1.51	0.040%
0.50	0.79	2.01	1.93	0.07	1.93	1.57	0.019%
0.75	0.90	2.01	1.92	0.08	1.92	1.64	0.007%
1.00	1.00	2.01	0.09	1.90	0.10	3.00	0.000%
1.25	1.08	2.01	1.89	0.11	1.89	1.78	0.005%
1.50	1.15	2.01	1.88	0.12	1.88	1.84	0.008%
1.75	1.21	2.01	1.87	0.13	1.87	1.91	0.010%
2.00	1.26	2.01	1.85	0.15	1.85	1.98	0.012%

Table 12. Global deviation GCI parameters for α=45%

k_2/k_1	k^*	$r_{1,2}$	p_t	Δp	p^*	FS	U_{num}
0.00	0.37	1.97	2.09	0.09	1.91	1.67	0.115%
0.25	0.57	1.97	2.05	0.05	1.95	1.45	0.038%
0.50	0.74	1.97	2.02	0.02	1.98	1.22	0.013%
0.75	0.88	1.97	1.98	0.02	1.98	1.21	0.005%
1.00	1.00	1.97	0.00	1.90	0.10	3.00	0.000%
1.25	1.11	1.97	1.92	0.08	1.92	1.61	0.004%
1.50	1.20	1.97	1.89	0.11	1.89	1.79	0.008%
1.75	1.28	1.97	1.86	0.14	1.86	1.94	0.011%
2.00	1.35	1.97	1.83	0.17	1.83	2.08	0.013%

Table 13. Global deviation GCI parameters for α=55%

k_2/k_1	k^*	$r_{1,2}$	p_t	Δp	p^*	FS	U_{num}
0.00	0.28	1.95	1.95	0.05	1.95	1.44	0.130%
0.25	0.50	1.95	1.96	0.04	1.96	1.35	0.040%
0.50	0.69	1.95	1.97	0.03	1.97	1.30	0.016%
0.75	0.85	1.95	1.98	0.02	1.98	1.26	0.005%
1.00	1.00	1.95	0.00	1.90	0.10	3.00	0.000%
1.25	1.13	1.95	1.99	0.01	1.99	1.16	0.003%
1.50	1.25	1.95	2.00	0.00	2.00	1.11	0.004%
1.75	1.35	1.95	2.01	0.01	1.99	1.15	0.006%
2.00	1.45	1.95	2.01	0.01	1.99	1.20	0.007%

Table 14. Global deviation GCI parameters for α=65%

k_2/k_1	k^*	$r_{1,2}$	p_t	Δp	p^*	FS	U_{num}
0.00	0.18	1.98	2.02	0.02	1.98	1.26	0.168%
0.25	0.43	1.98	2.03	0.03	1.97	1.34	0.044%
0.50	0.64	1.98	2.03	0.03	1.97	1.29	0.016%
0.75	0.83	1.98	2.02	0.02	1.98	1.24	0.005%
1.00	1.00	1.98	0.10	1.90	0.10	3.00	0.000%
1.25	1.16	1.98	2.02	0.02	1.98	1.21	0.003%
1.50	1.30	1.98	2.02	0.02	1.98	1.25	0.005%
1.75	1.43	1.98	2.03	0.03	1.97	1.33	0.007%
2.00	1.56	1.98	2.05	0.05	1.95	1.42	0.009%

5.3 CHARACTERISTIC TRENDS

Compiling all of the k^* from Table 8 through Table 14 shows a family of similar curves—roughly quadratic in form—relating k^* to both α and k_2/k_1, as illustrated in Figure 7.
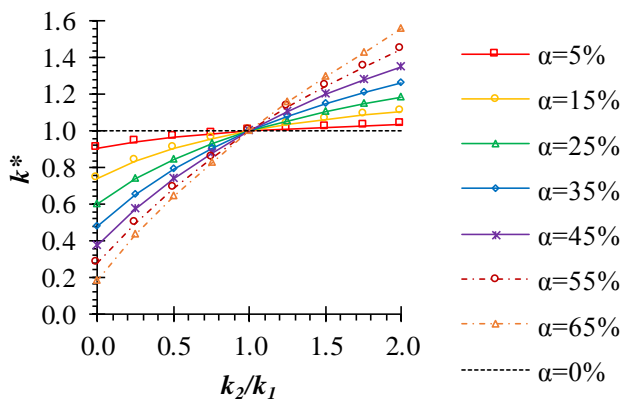
Figure 7. Dimensionless effective thermal conductivity characteristic curves

In Figure 7, it is clear that an increase in the pore material thermal conductivity leads to an increase in overall effective thermal conductivity of the composite material. Also, it is apparent from Figure 7 that an increase in pore size amplifies the relative effect of k_2 on k^*. All curves intersect at $(k_2/k_1=1.0, k^*=1.0)$, due to the fact that the condition of $k_2/k_1=1.0$ implies that the composite material behaves as a single homogeneous material from the perspective of steady-state thermal transport. Note that error bars on the k^* values are indistinguishable due to their relatively low values.

5.4 FUTURE WORKS

The study performed in this work has the potential to be extended to describe the effective thermal behavior in an analytical solution with prescribed uncertainty bounds. Likewise, the effects of pore topology and geometry on effective thermal responses of composite thermal material could be investigated as well as obtaining optimal thermal conductivity for microporous insulations. Similarly, such a study could have implications on the uncertainty incurred by mesh geometry. Further investigations could be made into analysis of transient effects or the implications of more than one pore material type in a given matrix.

6. CONCLUSION

This paper has presented a numerical approach to capturing the effective thermal transport behavior of a two-phase porous material with respect to pore phase thermal conductivity and pore size. It was shown that the employed FEM code was roughly second order accurate using the MMS code verification approach, and numerical uncertainty was estimated using the global deviation estimator GCI method. A trend was illustrated, tying the effective thermal conductivity of the overall medium to both relative pore size and relative pore thermal conductivity.

REFERENCES

[1] Ibrahim, T. K. and Rahman, M. M., 2013, "Study on effective parameter of the triple-pressure reheat combined cycle performance," Thermal Science, **17**(2), pp. 497-508.

[2] Nayak, J. and Mahto, D., 2014, "Effect of Gas Turbine Inlet Temperature on Combined Cycle Performance," *International Conference on Recent Innovations in Engineering & Technology*.

[3] Fathi, N., McDaniel, P., Forsberg, C., and de Oliveira, C., 2018, "Power Cycle Assessment of Nuclear Systems, Providing Energy Storage for Low Carbon Grids," Journal of Nuclear Engineering and Radiation Science, **4**(2), 020911.

[4] Fathi, Nima, Patrick McDaniel, Charles Forsberg, and Cassiano de Oliveira. "Nuclear Systems for a Low Carbon Electrical Grid." In 2016 24th International Conference on Nuclear Engineering, pp. V001T03A007-V001T03A007. American Society of Mechanical Engineers, 2016.

[5] Hunter, I., Daleo, J., Wilson, J., and Ellison, K., 1999, "Analysis of Hot Section Failures on Gas Turbines in Process Plant Service," *Proceedings of the 28th Turbomachinery Symposium*, **28**, pp. 9-20.

[6] Zohuri, Bahman, and Nima Fathi. "Thermal-Hydraulic Analysis of Nuclear Reactors."

[7] Salehnasab, B., Poursaeidi, E., Mortazavi, S. A., and Farokhian, G. H, 2016, "Hot corrosion failure in the first stage nozzle of a gas turbine engine," Engineering Failure Analysis, **60**, pp. 316-325.

[8] Rechard, Robert P., Teklu Hadgu, Yifeng Wang, Lawrence C. Sanchez, Patrick McDaniel, Corey Skinner, and Nima Fathi. Technical Feasibility of Direct Disposal of Electrorefiner Salt Waste. No. SAND2017-10554. Sandia National Lab.(SNL-NM), Albuquerque, NM (United States), 2017.

[9] Rechard, Rob P., Teklu Hadgu, Yifeng Wang, Larry C. Sanchez, Patrick McDaniel, Corey Skinner, Nima Fathi, Steven Frank, and Michael Patterson. "Feasibility of Direct Disposal of Salt Waste from Electochemical Processing of Spent Nuclear Fuel." arXiv preprint arXiv:1710.00855 (2017).

[10] Lai, G. Y., 2007, *High-Temperature Corrosion and Materials Applications*, ASM International, Novelty, OH.
[11] Rao, A. D, 2012, *Combined Cycle Systems for Near-Zero Emission Power Generation*, Woodhead Publishing Limited, Cambridge, UK.

[12] Ma, W., Li, X., Meng, X, Xue, Y, Bai, Y, Chen, W., and Dong, 2018, "Microstructure and Thermophysical Properties of $SrZrO_3$ Thermal Barrier Coating Prepared by Solution Precursor Plasma Spray," Journal of Thermal Spray Technology, **27**(7), pp. 1056-1063.

[13] McCay, M. H., Hsu, P.-f., Croy, D. E., Moreno, D., and Zhang, M., 2017, "The Fabrication, High Heat Flux Testing, and Failure Analysis of Thermal Barrier Coatings for Power Generation Gas Turbines," *Turbo Expo: Power for Land, Sea, and Air*, **6**():V006T24A008.

[14] Cernuschi, F., Bison, P., Mack, D. E., Merlini, M., Boldrini, S., Marchionna, S., Capelli, S., Concari, S., Famengo, A., Moscatelli, A., and Stamm, W., 2018, "Thermo-physical properties of as deposited and aged thermal barrier coatings (TBC) for gas turbines: State-of-the art and advanced TBCs," Journal of the European Ceramic Society, **38**(11), pp. 3945-3961.

[15] Irick, Kevin, and Nima Fathi. "Thermal Response of Open-Cell Porous Materials: A Numerical Study and Model Assessment." In ASME 2018 Verification and Validation Symposium, pp. V001T03A002-V001T03A002. American Society of Mechanical Engineers, 2018.

[16] Geuzaine, C. and Remacle, J.-F., 2009, "Gmsh: a three-dimensional finite element mesh generator with built-in pre- and post-processing facilities," International Journal for Numerical Methods in Engineering **79**(11), pp. 1309-1331.

[17] Oberkampf, W. L. and Roy, C. J., 2010, *Verification and Validation in Scientific Computing*, Cambridge University Press, Cambridge, UK.

[18] Roache, P. J., 2009, *Fundamentals of Verification and Validation,* Hermosa Publishers, Socorro, NM.

[19] Celik, I. B., Ghia, U., Roache, P. J., Freitas, C. J., Coleman, H., and Raad, P. E., 2008, "Procedure for Estimation and Reporting of Uncertainty Due to Discretization in CFD Applications," Journal of Fluids Engineering, **130**(7), pp. 0780011-0780014.

[20] Phillips, T. S. and Roy, C. J., 2016 "A New Extrapolation-Based Uncertainty Estimator for Computational Fluid Dynamics," Journal of Verification, Validation and Uncertainty Quantification, **1**(4), pp. 041006-1, 041006-13